ACS APPLIED MATERIALS & INTERFACES

www.acsami.org

Research Article

Residue-Driven Degradation and Its Stabilization in NaCl-Assisted WS_2 with 3R Stacking Enrichment

Lia Saptini Handriani, Hyeonsu Park, Zhe Gao, Jae-il Jang, and Won Il Park*

Cite This: *ACS Appl. Mater. Interfaces* 2026, 18, 39417−39428

Read Online

ACCESS | Metrics & More | Article Recommendations | Supporting Information

ABSTRACT: Salt-assisted chemical vapor deposition (CVD) enables large-grain synthesis of 2D transition-metal dichalcogenides, yet residual salts at the growth interface remain a critical bottleneck for ambient stability. Here, we investigate NaCl-assisted metal−organic CVD growth of WS_2 and reveal a coupled physical−chemical degradation mechanism driven by Na- and W-containing amorphous residues. Upon air exposure, these residues crystallize and mechanically disrupt the WS_2 layer while fostering a hygroscopic, Na-rich environment that drives oxidative breakdown of W−S bonds. Kinetic analysis establishes a thermally activated degradation process with an apparent activation energy of ∼0.22 eV, consistent with moisture-driven residue crystallization. We demonstrate that post-growth annealing (PGA) eliminates these residues and preserves the morphological integrity and optical emission characteristics over month-scale ambient storage. Beyond residue elimination, PGA also drives a pronounced 3R stacking enrichment in multilayer overgrowth regions. First-principles calculations reveal that interlayer Na^+ thermodynamically favors the 3R registry, so that 3R is selected during the early, Na-rich stage of annealing and kinetically locked once Na^+ is removed. These results establish residue management as a central design principle in salt-assisted 2D material synthesis.

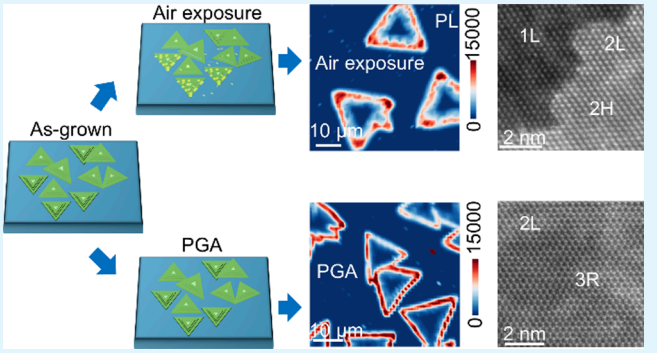

KEYWORDS: *WS_2, MOCVD, NaCl-assisted growth, ambient degradation, post-growth annealing, surface passivation, 3R stacking*

1. INTRODUCTION

Two-dimensional transition-metal dichalcogenides (2D TMDCs) constitute a promising class of layered semiconductors for electronics and optoelectronics, where atomic thickness enables strong electrostatic control, tunable band structures, and strong light−matter interactions.[1−5] Beyond crystallinity, achieving reliable device performance requires chemical and structural integrity of the grown layers, both of which are susceptible to contamination and structural disorder introduced during synthesis or postgrowth handling.[6−8] For instance, even weakly bound adsorbates or residue-derived impurities can disturb local doping and distort optical and electrical responses,[9,10] while structural disorder modulates band structure, nonlinear optical response, and electronic symmetry.[11,12] Realizing the full potential of 2D TMDCs therefore demands synthesis routes for large single-crystal domains, chemically clean interfaces, and controlled stacking configurations.

To move beyond exfoliation of small-scale flakes, chemical vapor deposition (CVD) and metal−organic CVD (MOCVD) have been widely explored for scalable synthesis of TMDCs.[13] Among these approaches, alkali-halide-assisted growth, particularly with NaCl,[14] has proved effective in producing micrometer-scale single-crystal domains at moderate growth temperatures.[15] This approach often yields large triangular flakes with good electrical and optical properties. However, the use of NaCl introduces residual species that persist at and around the WS_2/substrate interface and can compromise long-term stability. Previous work has shown that NaCl-assisted CVD-grown WS_2 is susceptible to ambient degradation via photo-induced and humidity-driven pathways.[16] However, the time-resolved kinetics, chemical origins, and effective post-growth mitigation of this instability have not yet been fully addressed.

Controlling the stacking order of as-grown multilayer WS_2 presents an equally important challenge. The 2H and 3R polytypes are nearly degenerate in energy (typically ∼ 1−10 meV per unit cell),[17] so conventional vapor-phase synthesis often yields mixed or turbostratic stacking. Consequently, simultaneously grown 2H- and 3R-stacked WS_2 multilayers readily emerge under standard CVD and physical vapor

Received: April 16, 2026
Revised: June 29, 2026
Accepted: June 29, 2026
Published: July 9, 2026

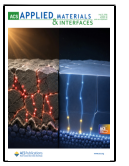

https://doi.org/10.1021/acsami.6c07675
ACS Appl. Mater. Interfaces 2026, 18, 39417−39428

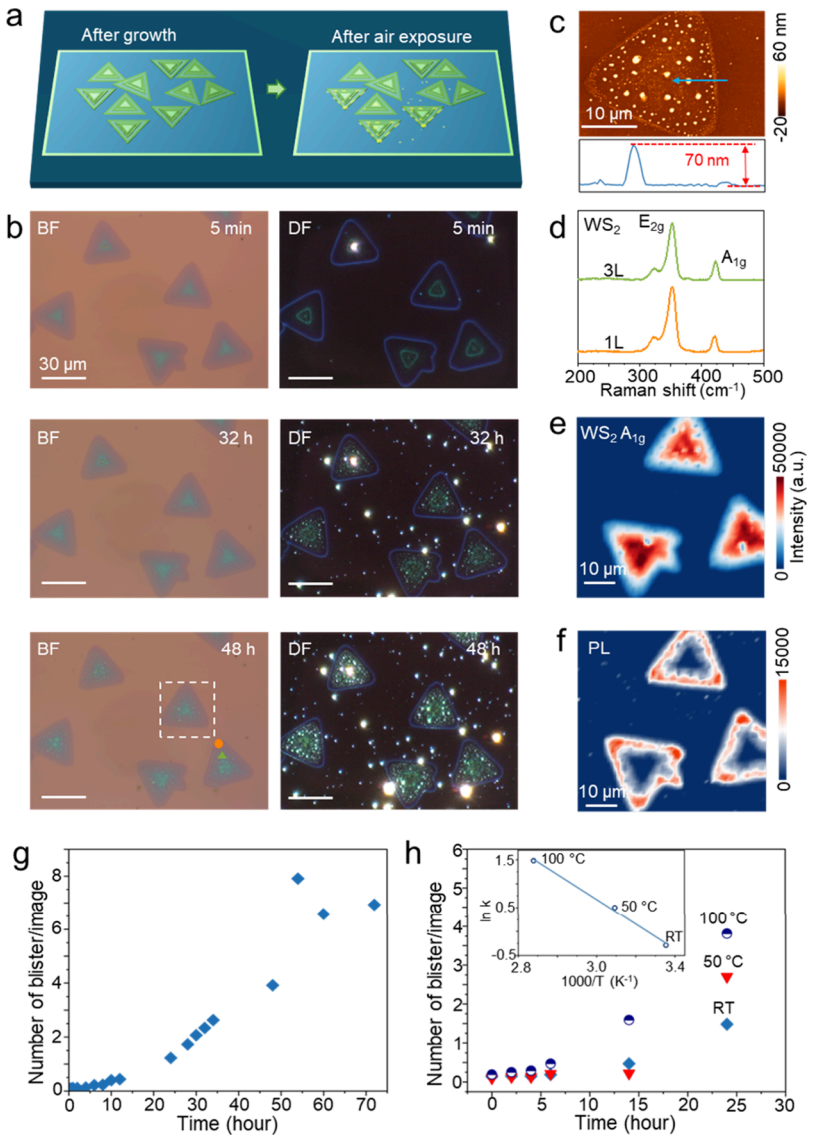

Figure 1. (a) Schematic of blister formation on NaCl-assisted WS_2 after air exposure. (b) Time-dependent BF and DF optical images showing progressive blister evolution at 5 min, 32 h, and 48 h. (c) AFM image and height profiles of an air-exposed flake, showing blister-like protrusions up to ~70 nm. (d) Representative Raman spectra from 1L and 3L regions (circle and triangle marks in the lower-left BF image of panel b). (e, f) Raman A_{1g} and PL maps showing spatially non-uniform optical response after degradation. (g) Time evolution of blister number ($\times 10^2$ per image) measured from the same optical image area (112 μm × 84 μm). (h) Temperature-dependent blister number ($\times 10^2$ per image) for the same image area at RT, 50 °C, and 100 °C; inset, Arrhenius analysis of the initial blister-formation rate.

deposition (PVD) conditions,[18,19] which can generate moiré superlattices.[20] Notably, post-growth thermal annealing under encapsulation has been shown to drive atomic reconstruction into fully commensurate R- or H-type configurations,[21] suggesting that post-growth treatments may offer a route to practical stacking control in TMDC multilayers.

Here, we investigate the stability and structural evolution of triangular WS_2 flakes grown by NaCl-assisted vertical MOCVD. We track their ambient evolution using correlated optical, spectroscopic, diffraction, and electron microscopy characterization. We reveal that as-grown flakes develop blister-like protrusions driven by crystallization of Na- and W-containing amorphous residues, which simultaneously creates a Na-rich alkaline surface environment that promotes oxidative breakdown of W−S bonds. We further demonstrate that post-growth annealing (PGA) in a sulfur-rich environment effectively suppresses these degradation pathways while promoting rhombohedral (3R) stacking in multilayer regions. By establishing a time-resolved picture of degradation and identifying a robust passivation route, this work offers a practical strategy for achieving environmental durability and stacking-controlled growth in salt-assisted 2D TMDC systems.

2. RESULTS AND DISCUSSION

2.1. Ambient Degradation Behavior of NaCl-Assisted WS_2

NaCl-assisted vertical MOCVD yielded isolated triangular WS_2 domains with lateral sizes in the tens-of-micrometers range on SiO_2/Si (see Methods; Figure S1). Despite this growth advantage, the as-grown NaCl-assisted WS_2 is unstable under ambient conditions. As shown schematically in Figure 1a, the initially clean flake surface gradually develops blister-like protrusions after air exposure. These protrusions arise from a residue-assisted process: residual Na- and W-containing

https://doi.org/10.1021/acsami.6c07675
ACS Appl. Mater. Interfaces 2026, 18, 39417−39428

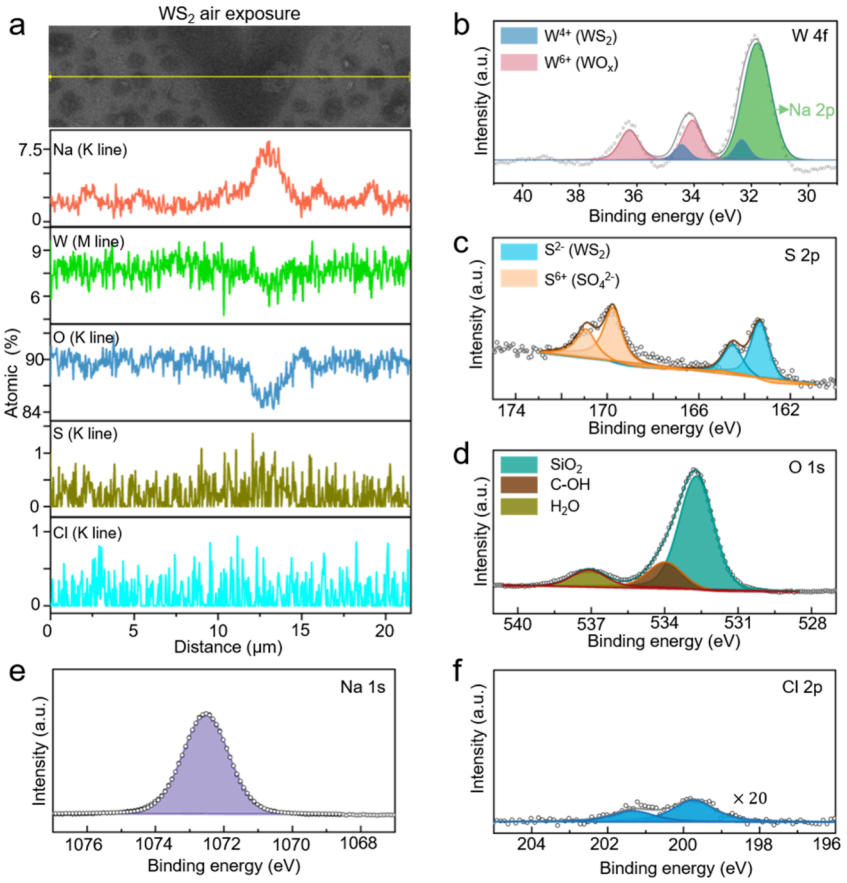

Figure 2. (a) Plan-view EDS line scan and elemental quantification across the degraded region, showing Na, W, and O enrichment with negligible S and trace Cl in the exposed outer residue. (b–f) High-resolution XPS spectra of W 4f, S 2p, O 1s, Na 1s, and Cl 2p, respectively.

amorphous species left after NaCl-assisted growth absorb atmospheric moisture and crystallize, and the accompanying volume expansion mechanically distorts the overlying atomically thin WS_2 layer. The detailed elemental and chemical evidence for this residue-assisted pathway is presented in Section 2.2.

Representative bright-field (BF) and dark-field (DF) optical microscopy (OM) images taken at 5 min, 32 h, and 48 h of exposure are shown in Figure 1b (see also Figure S2 for the full time-dependent sequence up to 72 h). At early times, only a few small protrusions are observed, whereas prolonged exposure leads to a clear increase in both the number and size of blisters across the sample (see Figure 1g for the quantitative analysis). These features are particularly evident in DF mode owing to their strong light-scattering. In the same dark-field images, scattering features are also observed outside the flake boundaries, on the surrounding exposed SiO_2/Si substrate, and become more pronounced with prolonged exposure. These outside features are not caused by deformation of the WS_2 layer but instead reflect residue-active species that also remain on the bare substrate after growth; their composition is examined in Section 2.2. The apparent decrease in small-protrusion count at later times (>50 h) reflects coalescence into larger blisters rather than surface recovery. It is noteworthy that degradation occurs preferentially over the basal plane rather than at crystal edges, consistent with previous reports of interior-site-initiated and humidity-assisted degradation in NaCl-assisted WS_2.[16]

To characterize the morphology of these features, atomic force microscopy (AFM) was performed on the region marked by the dashed box in Figure 1b (left bottom panel). The result shows the degraded surface containing pronounced blister-like protrusions with heights reaching ~ 70 nm, far exceeding the ~ 0.6 nm step height of the underlying WS_2 layer (Figure 1c), consistent with a residue-driven volumetric process rather than surface oxidation alone. Once such features develop, AFM-based layer-number determination becomes unreliable, as the measured step heights reflect blister-induced topographic distortion rather than the intrinsic WS_2 thickness.

The spectroscopic signatures of this degradation are further captured in the Raman and PL measurements. Representative Raman spectra confirm that the characteristic WS_2 vibrational modes remain detectable after ambient exposure (Figure 1d). However, the large-area Raman A_{1g} map (Figure 1e) reveals clear spatial inhomogeneity across the flake, demonstrating that the spectroscopic response is no longer uniform. The PL map (Figure 1f) shows a similar tendency, with locally distorted intensity distribution over the flake surface.

The temperature dependence of blister formation was also examined through controlled exposure experiments at RT, 50 °C, and 100 °C (Figures 1h and S3). As the exposure temperature increases, blisters nucleate and grow more rapidly, indicating that the degradation is a kinetically accelerated surface reaction process. To quantify this behavior, we estimated an apparent blister-formation rate k from the initial linear portion of the blister-count plot (Figure 1h) and

https://doi.org/10.1021/acsami.6c07675
ACS Appl. Mater. Interfaces 2026, 18, 39417−39428

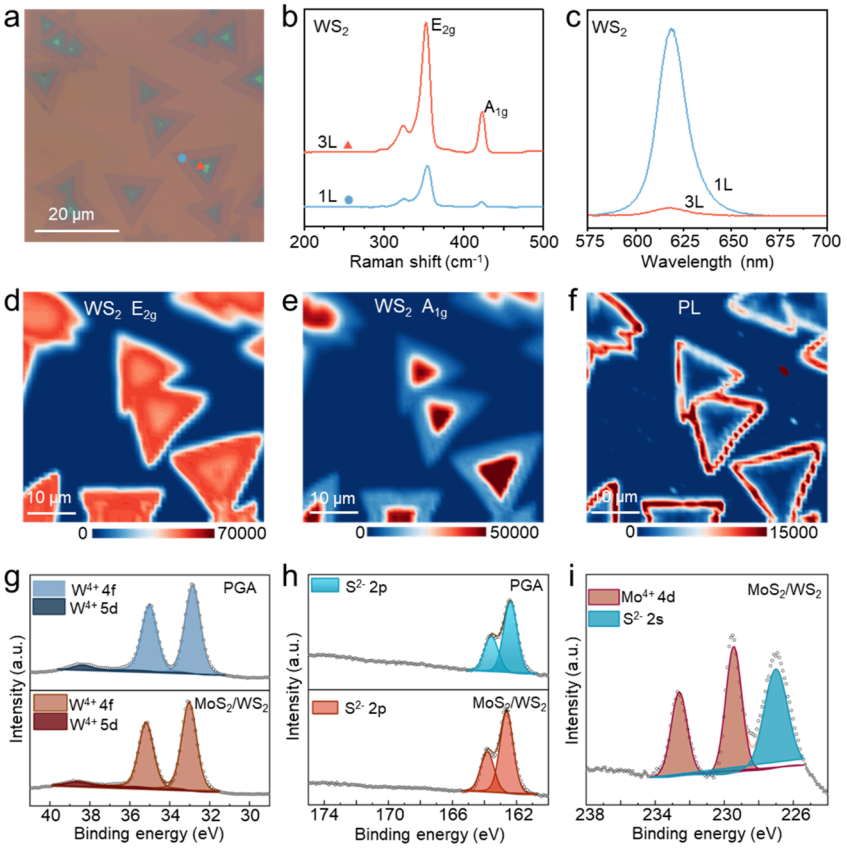

Figure 3. Characterization of NaCl-assisted WS_2 after PGA at 650 °C for 60 min under sulfur-rich conditions. (a) OM of a post-growth-annealed NaCl-assisted WS_2 flake. (b, c) Raman and PL spectra from representative 1L and 3L regions. (d, e) Raman E_{2g} and A_{1g} maps of the annealed flake. (f) PL map showing preserved thickness-dependent emission contrast. (g, h) W 4f and S 2p XPS spectra of PGA WS_2 and MoS_2/WS_2 heterostructures after ambient storage. (i) Mo 4d/S 2s XPS spectrum of the MoS_2/WS_2 heterostructure.

analyzed its temperature dependence using the Arrhenius relation,

$$k = A\exp\left(-\frac{E_a}{RT}\right)$$

where A is the pre-exponential factor, E_a is the activation energy, R is the gas constant, and T is the absolute temperature. The Arrhenius plot of ln k versus $1/T$ yielded an activation energy of approximately 21.6 kJ mol^{-1} (~0.22 eV), consistent with moisture-driven processes such as residue crystallization that are energetically accessible at near-ambient temperatures.

2.2. Chemical and Structural Origins of Blister Formation

The kinetic analysis above suggests a residue-assisted degradation pathway. Here we examine its chemical and structural origins. We propose that the ambient degradation is driven by Na- and W-containing amorphous residues left at the WS_2/SiO_2 interface and on the WS_2 and surrounding substrate surface following NaCl-assisted MOCVD growth. EDS analysis (Figure 2a) shows that residues at and around the degraded flake are enriched in Na and W, with negligible Cl content (Cl ≈ 0.03 at%), indicating that these residues are Na- and W-rich. Notably, the protrusion-containing region outside the WS_2 flake also retains substantial W together with Na and O, indicating that the outside protrusions originate from Na−W−O-containing residues deposited on the exposed SiO_2/Si substrate rather than from pure NaCl recrystallization, outward diffusion of WS_2 material, or intrinsic WS_2 blistering. Upon air exposure, these residues absorb atmospheric moisture and crystallize, as directly evidenced by the Na enrichment at blister sites in the EDS line profile (Figure 2a). The resulting volume expansion mechanically disrupts the overlying WS_2 layer, consistent with the ~ 70 nm blister heights that far exceed what surface oxidation alone could produce. Notably, the EDS line profile reveals that oxygen is locally depleted at the same Na-enriched blister positions, suggesting a Na-rich interior with oxidation confined primarily to the surface.

The chemical state of the degraded surface was further examined by XPS (Figure 2b−f). The combined spectral evidence indicates that the degraded surface has undergone extensive oxidation and moisture uptake, driven by the Na- and W-containing residues. The W 4f spectrum (Figure 2b) shows that after 7 days of air exposure, the W^{6+}/W^{4+} area ratio reaches ~ 2.6, indicating that WO_x formation has become the dominant chemical change.[16,22,23] The concurrent downshift of the W^{4+} doublet (~0.26 eV relative to pristine WS_2) indicates n-doping by residual Na^+, consistent with Na-bearing species at the interface. Consistent with the W 4f analysis, the S 2p spectrum (Figure 2c) shows that alongside the shifted W−S doublet, a high-binding-energy component at ~ 169−171 eV reveals sulfate (SO_4^{2-}) formation, signifying oxidative breakdown of W−S bonds.[23] The O 1s spectrum (Figure 2d) confirms that the surface is rich in adsorbed moisture and C−OH species,[24,25] consistent with a hygroscopic surface environment sustained by the Na- and W-containing residues that continuously trap atmospheric H_2O.[16] The Na 1s peak at 1072.53 eV (Figure 2e), characteristic of Na^+ in an oxide or

https://doi.org/10.1021/acsami.6c07675
ACS Appl. Mater. Interfaces 2026, 18, 39417−39428

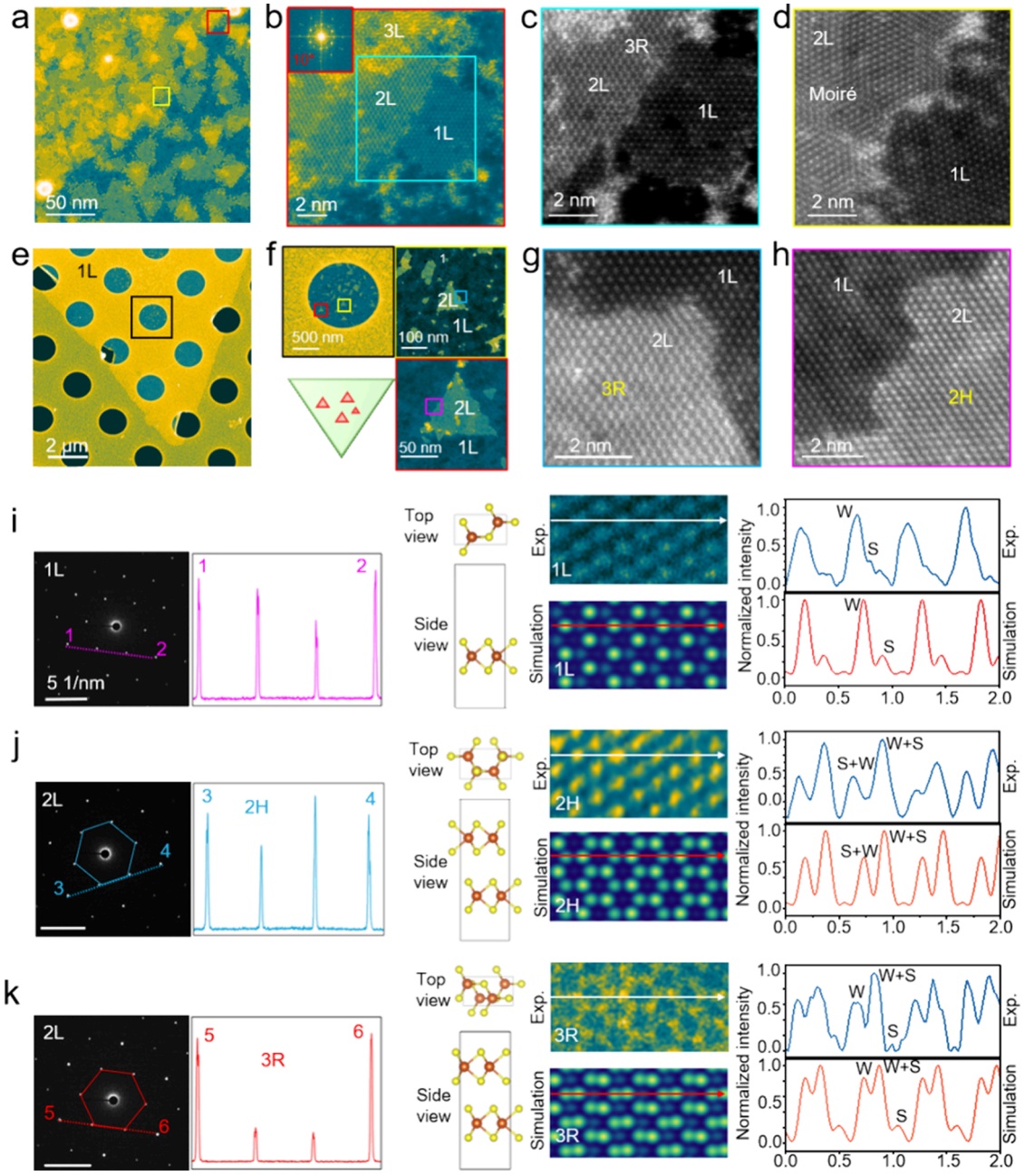

Figure 4. (a–d) Salt-free bilayer WS_2 exhibits a structurally heterogeneous overgrowth landscape dominated by rotationally disordered and incommensurate domains. (a) Low-magnification HAADF-STEM image with colored boxes marking the regions analyzed in panels b–d. (b) Enlarged 1L/2L/3L region, where fast Fourier transform (FFT) splitting reveals interlayer misorientation. (c) Atomic resolution image of a locally ordered 3R-like domain. (d) Atomic resolution image showing moiré contrast from an incommensurate interlayer relationship. (e) Low-magnification HAADF-STEM image of a large triangular flake with bilayer overgrowth. (f) Enlarged views of representative bilayer regions. (g, h) Atomic resolution images of representative 3R-like and 2H-like domains, respectively. (i–k) Diffraction patterns, structural models, experimental and simulated HAADF-STEM images, and corresponding line profiles for 1L WS_2 (i), 2H bilayer WS_2 (j), and 3R bilayer WS_2 (k).

hydroxide environment, and the near-absent Cl 2p signal (Figure 2f) together confirm that the blister surface is covered by NaO_x-type species rather than recrystallized NaCl, in agreement with the EDS observations. It should be noted that the XPS signal integrates contributions from both the WS_2 flake and the surrounding bare SiO_2 substrate, so the W and Na signals are likely to include contributions from residues on the substrate in addition to those directly associated with the WS_2 lattice.

These observations collectively suggest that Na- and W-containing amorphous residues crystallize upon air exposure and mechanically disrupt the WS_2 layer, while the resulting Na-rich alkaline surface environment promotes oxidative breakdown of W–S bonds, with ambient O_2 and H_2O sustaining further attack at the generated defect sites.

2.3. Suppression of Degradation by PGA

The coupled physical–chemical degradation mechanism motivates the question of how such degradation can be effectively suppressed. We demonstrate here that PGA in a sulfur-rich environment achieves this goal. Before any ambient exposure, the WS_2 flakes were subjected to immediate PGA at

https://doi.org/10.1021/acsami.6c07675
ACS Appl. Mater. Interfaces 2026, 18, 39417–39428

650 °C for 60 min under sulfur-rich conditions, and the results are summarized in Figure 3. This temperature was selected from a comparison of PGA at 600, 650, and 700 °C followed by 1 day of ambient exposure (Figure S4): at 600 °C — below the 635 °C growth temperature — passivation was only partial and residual post-exposure damage remained, while at 700 °C thermally induced morphological degradation of the flakes was observed; 650 °C uniquely retained a well-defined triangular morphology after exposure. The annealing treatment preserves both the structural integrity and optical properties of the flakes, as confirmed by the well-defined triangular morphology in the OM image (Figure 3a). Raman and PL spectra collected from the monolayer and multilayer regions (circle and triangle marks in Figure 3a) show the characteristic thickness-dependent responses of WS_2 (Figure 3b,c), consistent with the layer contrast seen in the OM image (Figure 3a). Consistent with these point spectra, Raman mapping of the E_{2g} and A_{1g} modes (Figure 3d,e) shows uniform intensity distributions across the flake, while the PL map (Figure 3f) displays the expected thickness-dependent emission contrast, with stronger emission from the monolayer region.

To further assess the local strain and chemical-environment heterogeneity before and after PGA, spatially resolved Raman spectroscopy was performed by mapping the E_{2g} and A_{1g} peak positions together with the Raman peak separation, $\Delta\omega = \omega_{A_{1g}} - \omega_{E_{2g}}$ (Figure S5). Because the E_{2g} mode shifts primarily with strain whereas the A_{1g} mode — and hence $\Delta\omega$ — responds more strongly to doping and the local chemical environment, the E_{2g} peak-position map serves as the primary strain indicator and the A_{1g} and $\Delta\omega$ maps report doping/chemical-environment variation. Without PGA, the air-exposed sample with blister-like protrusions exhibits a spatially nonuniform E_{2g} peak-position distribution across monolayer regions, indicating heterogeneous local strain; the A_{1g} position and $\Delta\omega$ (66.0–68.6 cm^{-1} across monolayer regions) vary in parallel, consistent with doping/chemical-environment heterogeneity introduced by the Na-rich residues, blistering, and delamination. In contrast, the PGA-treated sample shows a uniform E_{2g} peak-position map, indicating homogeneous strain, together with uniform A_{1g} and $\Delta\omega$ maps ($\Delta\omega$ = 68.6 cm^{-1} for monolayer and 70.0 cm^{-1} for trilayer regions). These results indicate that PGA suppresses the development of blister-induced local Raman inhomogeneity by eliminating the residue-driven origin of delamination before ambient exposure. Therefore, PGA should not be interpreted as a post-damage process that completely relaxes pre-existing blister-induced strain; rather, it prevents the formation of such strain/disorder heterogeneity.

XPS analysis further confirms the chemical effectiveness of these treatments (Figure 3g–i). In sharp contrast to the air-exposed samples, the annealed WS_2 retains pristine W^{4+} and S^{2-} signatures with no detectable W^{6+} or sulfate (~169 eV) contributions, confirming effective suppression of both W and S oxidation.[26,27] A similar effect is observed for MoS_2 heterostructure capping, in which an MoS_2 overlayer grown without NaCl serves as an alternative passivation route. In this case, slight XPS W 4f and S 2p peak shifts reflect interfacial charge transfer rather than chemical degradation, and the MoS_2 capping layer itself remains chemically intact, retaining a pure Mo^{4+} state with no detectable MoO_x features.[28]

Suppression of the Na- and W-containing residues responsible for degradation is also clearly confirmed. While the air-exposed sample shows a prominent Na 1s signal alongside a weak but detectable Cl 2p signal, both PGA and MoS_2 heterostructure capping substantially reduce the Na 1s intensity, with Cl 2p becoming further suppressed after PGA and virtually absent after MoS_2 capping (Figure S6a,b). Consistently, the C–OH and adsorbed H_2O components observed in the O 1s spectrum of the air-exposed sample are also absent in both treated samples (Figure S6c). The long-term stability of the passivated flakes is further demonstrated by month-scale ambient storage (Figures S7 and S8), where PGA-treated samples maintain stable emission at 623 nm over 3 months, in contrast to the progressive 12 nm red-shift (626 to 638 nm) observed without PGA within 30 days. The NaCl loading itself also influences residue formation: across 0.2, 0.4, and 0.6 g NaCl (Figure S9), the residue-driven protrusion density increases monotonically but supralinearly with NaCl loading (216.5 ± 39.0, 424.5 ± 86.2, and 824.0 ± 105.8 blisters per image at 0.2, 0.4, and 0.6 g, respectively; N = 6), with a 3-fold increase in NaCl loading raising the protrusion density nearly 4-fold, while the as-grown morphology deteriorates at lower loadings — the 0.2 g condition yields poorly defined, rounded domains rather than the well-defined triangular flakes obtained at 0.6 g. This trade-off indicates that reducing the NaCl loading cannot simultaneously suppress residues and preserve growth quality; PGA therefore remains the more practical strategy for suppressing residue-driven degradation while maintaining well-defined WS_2 morphology.

2.4. NaCl-Mediated Stacking Alignment and PGA-Driven 3R Enrichment in Multilayer WS_2

Beyond passivation, NaCl-assisted growth and subsequent PGA also govern stacking configuration of multilayer WS_2 overgrown regions. We first establish a crystallographic baseline using conventionally grown, salt-free WS_2 as a reference. Atomic-resolution high-angle annular dark-field scanning transmission electron microscopy (HAADF-STEM) reveals that the overgrown mulitlayer regions do not form a uniform commensurate stacking configuration and instead exhibit a structurally heterogeneous distribution dominated by rotationally misaligned and turbostratic domains (Figure 4a). FFT from the red-box region shows broadened and partially split diffraction patterns (Figure 4b), indicating substantial rotational disorder with an interlayer twist of about 10°. The cyan-box region in Figure 4b shows a small locally ordered 3R-like domain (Figure 4c), though such ordered stacking remains spatially isolated. Moiré contrast observed in the yellow-box region (Figure 4d) confirms the coexistence of an incommensurate interlayer relationship caused by a larger rotational mismatch. These observations indicate that, without NaCl, multilayer overgrowth is dominated by twisted and turbostratic stacking with poor registry control. This is attributed to the tendency of independently nucleated WS_2 domains to overgrow with random interlayer orientations under standard vapor-phase growth conditions.

In contrast to the salt-free reference, samples grown with NaCl form large triangular WS_2 domains with markedly improved interlayer registry. Atomic-resolution STEM directly resolves ordered bilayer domains in these samples (Figure 4g,h), despite the presence of some void defects attributed to ambient degradation prior to STEM analysis (Figures 4e,f and S10b,c). Nevertheless, both 2H- and 3R-like stacking configurations coexist within these ordered regions, indicating that Na^+ improves interlayer alignment during overgrowth

https://doi.org/10.1021/acsami.6c07675
ACS Appl. Mater. Interfaces 2026, 18, 39417–39428

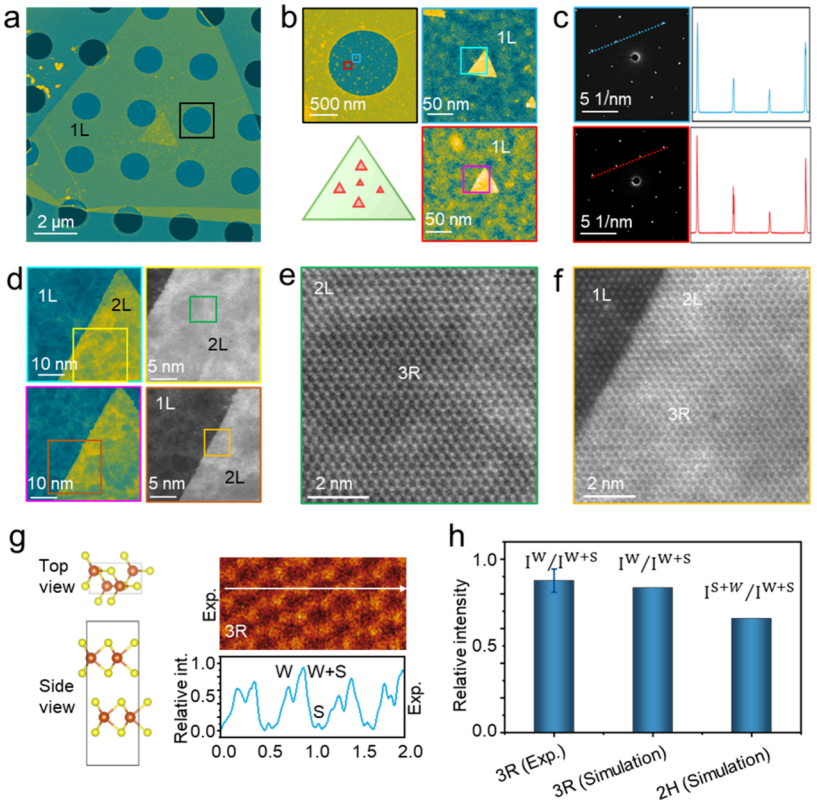

Figure 5. (a) Low-magnification HAADF-STEM image of PGA-treated NaCl-assisted WS_2. (b) Enlarged HAADF-STEM views of representative bilayer regions, together with the schematic indicating the analyzed positions. (c) Diffraction patterns and corresponding spot intensity profiles characteristic of 3R stacking. (d) Enlarged STEM views of selected bilayer edge regions showing well-defined 1L/2L boundaries. (e, f) Atomic-resolution HAADF-STEM images of representative PGA-treated bilayer regions with uniform 3R-like contrast. (g) Structural model, experimental HAADF-STEM image, and projected intensity profile for a representative 3R-stacked bilayer region. (h) Statistical comparison of the relative intensity ratio extracted from the line profiles.

without yet selecting a single polytype at the growth stage (an origin we examine below). This coexistence is consistent with the near-energetic degeneracy of the two configurations (~1−10 meV per unit cell)[17] and with the previously reported role of alkali-metal species in biasing interlayer registry toward specific polytypes in related layered systems.[21,29] The stacking assignments are further supported by the combined analysis of diffraction patterns, HAADF-STEM contrast, and multislice simulations (Figure 4i−k). The monolayer region shows a single unsplit 6-fold diffraction pattern consistent with single-crystalline 1L WS_2 (Figure 4i). In the commensurate bilayer regions, 2H and 3R configurations are distinguished by their diffraction spot intensity ratios and atomic-column contrast patterns, both of which agree closely with the respective multislice simulations (Figure 4j,k). The 3R region additionally exhibits suppressed first-order diffraction intensity relative to the second-order set, providing further confirmation of the stacking assignment.[30]

Post-growth sulfur-assisted annealing further refines this mixed-phase distribution. STEM analysis of the annealed samples reveals a markedly increased incidence of 3R stacking signatures relative to the as-grown state, accompanied by a visibly cleaner crystal morphology with significantly reduced void defects (Figures 5a,b, and S10e,f). More importantly, diffraction from multiple bilayer regions consistently exhibits the intensity distribution characteristic of 3R stacking, in clear contrast to the mixed 2*H*/3R distribution observed prior to annealing. HAADF-STEM images also reveal laterally extended bilayer domains with uniform 3R-like contrast and no obvious local admixture of 2H registry in the analyzed regions (Figure 5c−f). A representative projected intensity profile agrees closely with the 3R structural model, with the statistical weak-to-strong peak intensity ratio consistently matching the 3R simulation more closely than the 2H configuration (Figure 5g,h). To quantify this structural evolution statistically, we analyzed SAED patterns from N = 10 independently sampled multilayer regions per condition (Figure S11). For each region, the I^{inner}/I^{outer} intensity ratio was measured along six crystallographic line profiles and averaged into a single representative ratio per region, following the classification approach of Zeng et al.[30] The 2H- and 3R-classified regions formed two well-separated groups (mean ratios of ~ 0.84 and ~ 0.20−0.27, respectively), confirming an unambiguous distinction between the two stacking types. Before PGA, the commensurate domains were evenly split (5 of 10 regions 2H, 5 of 10 3R), indicating that, despite the thermodynamic preference for 2H, Na^+ present during NaCl-assisted growth already stabilizes a substantial 3R population prior to annealing. This represents just a partial expression of the underlying Na-induced preference, with full enrichment achieved only after annealing. After PGA, 9 of 10 regions were classified as 3R, indicating that PGA results in a multilayer population that is predominantly 3R-stacked. The distribution of representative ratios across the 10 sampled regions is broad before PGA and shifts markedly toward lower values after PGA, consistent with the population-level

https://doi.org/10.1021/acsami.6c07675
ACS Appl. Mater. Interfaces 2026, 18, 39417−39428

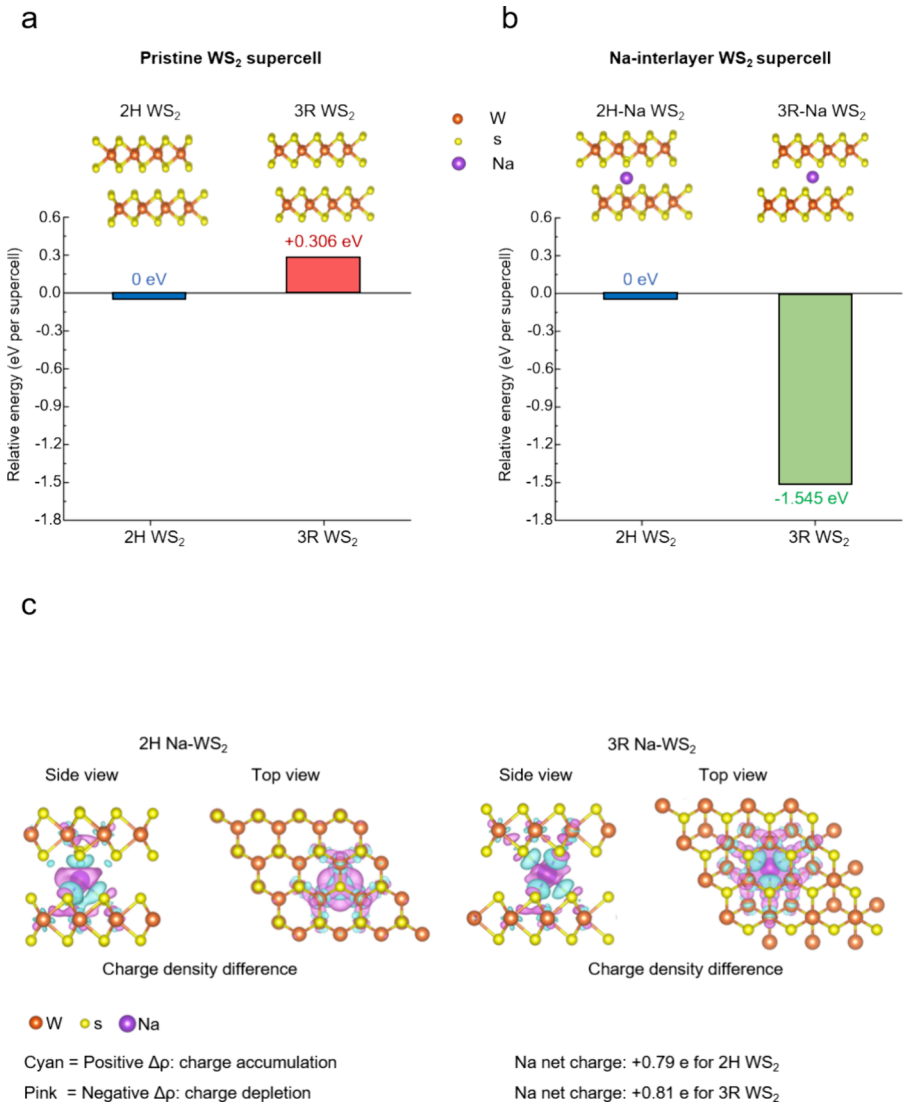

Figure 6. DFT total-energy and charge density difference analysis of bilayer WS_2 with and without interlayer Na. (a) Relative total energies of pristine 2H and 3R WS_2 supercells (reference: 2H); 2H is favored by ∼9.6 meV per formula unit (∼0.31 eV per 4 × 4 supercell). (b) Relative total energies of 2H Na−WS_2 and 3R Na−WS_2 supercells (reference: 2H Na−WS_2); 3R is favored by ∼48 meV per formula unit (∼1.55 eV per 4 × 4 supercell). (c) Charge density difference (CDD) isosurfaces (isovalue = 0.001 e/bohr^3) for 2H Na−WS_2 and 3R Na−WS_2 in side and top views; cyan: charge accumulation ($\Delta\rho > 0$); pink: charge depletion ($\Delta\rho < 0$). Bader charges: Na to WS_2 transfer of +0.79 e (2H Na−WS_2) and +0.81 e (3R Na−WS_2). Atom colors: W (orange), S (yellow), Na (purple).

transition from a mixed 2*H*/3R state to a predominantly 3R-stacked configuration (Figure S12b). Taken together, these observations indicate that PGA does not merely heal surface disorder but drives a substantial structural reorganization of the overgrowth toward a predominantly 3R-stacked configuration.

It is noteworthy that this 3R enrichment is not immediately expected, given that 2H is the thermodynamically more stable polytype in pristine WS_2.[17,29] Our own pristine calculations place the 2*H*/3R difference in this same near-degenerate regime (2H favored by ∼ 9.6 meV per formula unit, 0.31 eV per 4 × 4 supercell; Figure 6a). Building on these calculations, we propose the following Na^+-centered, stage-resolved mechanism. Its thermodynamic basis is established directly by the DFT results above; the temporal sequence below remains a proposal pending in situ verification. In the as-grown state, NaCl-assisted WS_2 contains commensurate but mixed 2*H*/3R domains (Figures 4g,h, S11, and S12) together with residual Na^+ and point defects such as sulfur vacancies, as evidenced by XPS. During the early, Na-rich stage of PGA, interlayer Na thermodynamically stabilizes the 3R registry (∼48 meV per formula unit, 1.55 eV per 4 × 4 supercell; Figure 6b), and the elevated temperature activates registry reorganization toward this Na-preferred 3R configuration — by interlayer sliding where adjacent layers already share a common orientation (assisted by a Na-induced reduction of the sliding barrier; Figure S13) and by atomic rearrangement where they do not, as in the conversion of 2H to 3R, which differ in interlayer azimuthal orientation. During the later stage, the sulfur-rich atmosphere compensates sulfur vacancies and suppresses oxidation (Sections 2.2−2.3) while residual Na^+ is progressively removed; the system then returns to its near-degenerate intrinsic landscape (Figure 6a), but the 3R domains formed earlier are kinetically locked, since reverting them to 2H requires this azimuthal atomic rearrangement, whose barrier is not overcome under the mild conditions once the Na that favored 3R has been removed. The 3R-enriched state

https://doi.org/10.1021/acsami.6c07675
ACS Appl. Mater. Interfaces 2026, 18, 39417−39428

observed after PGA is therefore attributed to Na-induced thermodynamic registry selection during early stage annealing, followed by kinetic trapping once Na is removed, rather than to defect-controlled polytype energetics. Direct confirmation of the proposed temporal sequence will require in situ characterization during annealing.

We now detail the calculations underlying this mechanism. Using static total-energy DFT, we compared 2H and 3R bilayer registries with and without an interlayer Na atom (Figure 6a,b). In the pristine, Na-free bilayer, 2H is favored over 3R by ∼ 9.6 meV per formula unit (0.31 eV per 4 × 4 supercell; Figure 6a), placing the intrinsic 2*H*/3R difference in the same near-degenerate regime as previously reported.[17,29] With an interlayer Na atom present, this preference reverses, the 3R configuration becoming favored over 2H by ∼ 48 meV per formula unit (1.55 eV per 4 × 4 supercell; Figure 6b). As this value reflects a single Na atom within a 4 × 4 bilayer supercell, it represents a strong local binding preference of interlayer Na for the 3R environment rather than a bulk per-formula-unit quantity, and its influence scales with local Na content. Na incorporation thus does not merely facilitate kinetic access to 3R; it makes 3R the locally preferred registry.

Charge density difference (CDD) analysis and Bader charge partitioning (Figure 6c) show net electron donation from Na to the WS_2 sublattice in both registries, of similar magnitude (+0.79 e in 2H, + 0.81 e in 3R). The near-identical transfer indicates that the differential stabilization does not arise from the amount of donation. Rather, the top-view CDD isosurfaces (Figure 6c) show the donated charge to be more symmetrically distributed across the surrounding S atoms in the 3R configuration, which we interpret as the 3R interlayer geometry providing a more balanced electrostatic environment for the donated charge. This interpretation is mechanistically consistent with the electron-donation-driven 3R stabilization reported for Na-intercalated MoS_2.[29]

Structural analysis further shows that interlayer Na is accommodated with less perturbation in 3R: upon Na incorporation the local S−S interlayer gap expands by +0.142 Å in 3R versus +0.436 Å in 2H, while far-field regions remain near their pristine values, confirming a local rather than uniform distortion. We regard this geometric size-matching as a secondary effect accompanying, rather than driving, the dominant electronic stabilization.

3. CONCLUSION

This study provides a comprehensive understanding of the ambient instability of NaCl-assisted WS_2 and identifies an effective mitigation strategy. We demonstrate that as-grown flakes develop blister-like protrusions driven by crystallization of Na- and W-containing amorphous residues, which mechanically disrupt the WS_2 layer while simultaneously creating a Na-rich alkaline surface environment that promotes oxidative breakdown of W−S bonds. PGA in a sulfur-rich environment effectively suppresses this degradation by removing these residues, ensuring month-scale environmental stability. Importantly, PGA also drives structural reorganization of the multilayer overgrowth toward a predominantly 3R-stacked configuration. First-principles calculations attribute this 3R enrichment to a Na^+-induced thermodynamic preference for the 3R registry, whereby 3R is selected while residual Na^+ is present during the early stage of annealing and is then kinetically locked once Na^+ is removed. These findings highlight the importance of post-growth residue management in salt-assisted synthesis and offer a practical pathway toward environmentally stable, 3R-enriched 2D TMDC systems.

EXPERIMENTAL SECTION

4.1. NaCl-Assisted MOCVD Growth of WS_2

Triangular WS_2 flakes were synthesized on SiO_2/Si substrates using a custom-built vertical cold-wall MOCVD reactor equipped with a rotating graphite susceptor. Tungsten hexacarbonyl ($W(CO)_6$, WHC) and diethyl sulfide ($(C_2H_5)_2S$, DES) served as tungsten and sulfur precursors, respectively. The solid WHC and liquid DES were maintained in temperature-controlled bubblers at 30 and 55 °C, respectively, and delivered into the reactor using Ar as a carrier gas.[31,32]

To promote large-domain growth, a NaCl-assisted strategy was employed by placing a circular crucible containing 0.6 g of NaCl (Sigma-Aldrich, ≥ 99%) at the center of the susceptor (Figure S1a). Growth was conducted at 635 °C and 5 Torr for 20 min, with WHC and DES introduced at equal flow rates of 6 sccm each under a background flow of 250 sccm Ar and 10 sccm H_2. The as-grown NaCl-assisted WS_2 flakes were used directly for ambient degradation studies and post-growth annealing experiments described below.

4.2. PGA

PGA in a sulfur-rich environment was performed in the same vertical cold-wall MOCVD reactor immediately after WS_2 growth, without breaking vacuum or exposing the sample to ambient atmosphere. Prior to annealing, the NaCl source crucible was physically removed from the susceptor to eliminate any further salt vapor contribution during the thermal treatment. The reactor was then purged with 250 sccm Ar for 5 min at room temperature to flush residual precursor and salt-derived vapor species from the chamber before initiating the annealing sequence.

Annealing was carried out at 650 °C for 60 min under a sulfur-rich atmosphere supplied by DES (2 sccm) with a background flow of 250 sccm Ar and 10 sccm H_2 at 5 Torr — conditions otherwise identical to those used during WS_2 growth. The temperature was ramped to the target value at 10 °C °C min^{-1} and held for 60 min, after which the DES flow was terminated and the sample was cooled naturally to below 100 °C under continued Ar/H_2 flow before unloading. The annealing temperature dependence of the passivation outcome is presented in Figure S4.

For comparison, a subset of WS_2 samples was capped with a MoS_2 overlayer by performing a second MOCVD step using $Mo(CO)_6$ and DES under identical reactor conditions (650 °C, 5 Torr, 250 sccm Ar, 10 sccm H_2), as described in detail in our previous report.[33] These WS_2/MoS_2 heterostructure samples served as an alternative passivation reference to evaluate the relative effectiveness of chemical encapsulation versus PGA in suppressing the coupled degradation pathways.

4.3. Optical and Structural Characterization

4.3.1. OM and AFM. The surface morphology and layer contrast of as-grown and annealed WS_2 flakes were examined by optical microscopy (OM; Olympus BX51) in both bright-field (BF) and dark-field (DF) modes. Time-dependent ambient degradation was tracked by acquiring correlated BF/DF image sequences on the same flake at controlled intervals and temperatures. Atomic force microscopy (AFM) was performed in tapping mode to determine step heights, quantify blister-like protrusion dimensions, and verify the layer number of as-grown and annealed flakes. AFM topography profiles were used to confirm the monolayer step height (∼0.6 nm) and to assess the surface topographic evolution during ambient exposure.

4.3.2. Raman and Photoluminescence Spectroscopy. Room-temperature Raman and photoluminescence (PL) measurements were performed using a micro-Raman system (Dongwoo Optron) equipped with a 532 nm continuous-wave excitation laser and 50×/100× objective lenses. Spectra were acquired in backscattering geometry with a laser power below 0.5 mW to avoid laser-induced

https://doi.org/10.1021/acsami.6c07675
ACS Appl. Mater. Interfaces 2026, 18, 39417−39428

heating or photodegradation. Raman and PL mapping was carried out on predefined grids with a step size of 0.5 μm to resolve spatial variations in the E_{2g} and A_{1g} mode intensities and peak positions, as well as the excitonic PL emission, across the flake interior and edges. Spectral data sets were processed using baseline subtraction followed by multi-Gaussian peak fitting to deconvolute overlapping modes and obtain reliable intensity and peak-position maps.

4.3.3. X-Ray Photoelectron Spectroscopy. X-ray photoelectron spectroscopy (XPS) measurements were performed using a Thermo Scientific K-Alpha Plus equipped with a monochromatic Al Kα X-ray source ($h\nu$ = 1486.6 eV) under ultrahigh-vacuum chamber with a base pressure below 5×10^{-9} Torr. High-resolution spectra were acquired for the W 4f, S 2p, O 1s, Na 1s, and Cl 2p core levels. All binding energies were referenced to the adventitious C 1s peak at 284.8 eV. Spectral deconvolution was performed using the open-source KherveFitting package, which provides multiple background subtraction methods and peak models.[34] The Smart background was adopted because it automatically applies a linear background when the spectral baseline decreases with increasing binding energy and a Shirley-type background when it increases, thereby enabling adaptive treatment of the inelastic background across the entire binding-energy range of each spectrum. Peak envelopes were modeled using the SGL (sum of Gaussian and Lorentzian) line shape, selected as a practical approximation for the mixed instrumental broadening, disorder, and lifetime contributions that determine the observed core-level profiles. All fits were carried out using the Levenberg–Marquardt least-squares routine implemented in KherveFitting, and fit quality was evaluated from the residuals together with the reported R^2 and reduced chi-square (χ^2) values.

4.3.4. Scanning Transmission Electron Microscopy. Atomic-scale stacking order and interfacial structure of the as-grown and annealed WS_2 bilayer regions were examined by spherical-aberration-corrected high-angle annular dark-field scanning transmission electron microscopy (HAADF-STEM; JEOL JEM-ARM200F) operated at 80 kV. HAADF-STEM images were acquired with a probe convergence semiangle of 20 mrad and an annular detector spanning 60–200 mrad. The stacking registry (2H vs 3R) was assigned from the characteristic three-intensity pattern (S, W, and W + S columns) visible in the plan-view images, following established HAADF contrast criteria for bilayer TMDCs.[35,36]

4.3.5. HAADF-STEM Image Simulation. To validate the experimentally assigned stacking configurations, multislice HAADF-STEM image simulations were performed using the Dr. Probe software package.[37] Simulation parameters were matched to the experimental imaging conditions: acceleration voltage 80.00 kV, probe convergence semiangle 20.0 mrad, and HAADF detector collection range 60.0–200.0 mrad. Atomic supercells for 2H- and 3R-stacked bilayer WS_2 were constructed from crystallographic data and discretized into slices along the beam direction (Z-axis) to model electron wave propagation through the full layer stack. Simulated images were directly compared with experimental HAADF-STEM data to confirm the stacking assignments reported in Section 2.4.

4.3.6. Density Functional Theory Calculations. Density functional theory calculations were performed using the Quantum ESPRESSO package.[38,39] The exchange-correlation interaction was described using the Perdew–Burke–Ernzerhof functional within the generalized gradient approximation,[40] and projector augmented-wave pseudopotentials were used for W, S, and Na atoms.[41] van der Waals interactions were included using the Grimme D3 dispersion correction with Becke–Johnson damping.[42,43] Marzari–Vanderbilt cold smearing was used for the electronic occupations.

The plane-wave cutoff energy, Brillouin-zone sampling, and out-of-plane lattice parameter were converged using the pristine bilayer WS_2 primitive cell. The wave function cutoff was tested from 40 to 90 Ry with the charge-density cutoff maintained at eight times the wave function cutoff; cutoff energies of 70 and 560 Ry were adopted for the wave functions and charge density, respectively. The k-point mesh was tested from $6 \times 6 \times 1$ to $18 \times 18 \times 1$, and a $12 \times 12 \times 1$ mesh was used for the primitive cell; for the 4×4 supercell calculations, a scaled $3 \times 3 \times 1$ mesh was used. The out-of-plane lattice parameter was tested from 15 to 30 Å, and a value of 25 Å was adopted to minimize artificial interactions between periodic slab images.

Pristine bilayer WS_2 was modeled using a six-atom primitive cell containing two W atoms and four S atoms. The 2H and 3R stacking configurations were constructed using the same in-plane lattice parameter and relaxed with fixed cell parameters. During relaxation, the in-plane coordinates of W and S atoms were fixed to preserve the stacking registry, while their out-of-plane coordinates were allowed to relax. Structural relaxation of the pristine primitive cells was converged to a force threshold of 2.6×10^{-3} eV/Å for both 2H and 3R configurations. For Na-containing calculations, a 4×4 bilayer WS_2 supercell ($W_{32}S_{64}Na_1$) was used. Na atoms were allowed to relax in all Cartesian directions, while W and S atoms were relaxed only along the out-of-plane direction. Structural relaxation of the Na-intercalated supercells was continued until no further reduction in total force was observed; the final residual forces are 0.069 eV/Å (2H Na-WS_2) and 0.054 eV/Å (3R Na-WS_2), consistent with the behavior of light alkali intercalants in large vdW supercells where the soft interlayer potential limits force convergence. The total-energy difference of $\sim$ 1.55 eV between the two registries far exceeds any plausible force-related uncertainty, and the qualitative conclusion is independently corroborated by charge density difference analysis and Bader charge partitioning.

The relative registry stability was evaluated as $\Delta E = E(3R) - E(2H)$, computed at fixed supercell composition with identical k-point mesh, smearing parameters, and cutoff energies across compared structures to ensure cancellation of systematic errors. Charge density differences were computed as

$$\Delta\rho = \rho(\mathrm{Na - WS_2}) - \rho(\mathrm{WS_2}) - \rho(\mathrm{Na})$$

where all three densities were evaluated using identical cell parameters, grids, and pseudopotentials. CDD isosurfaces were visualized at an isovalue of 0.001 e/bohr^3. Atomic charges were obtained using Bader charge partitioning.[44]

■ ASSOCIATED CONTENT

Supporting Information

The Supporting Information is available free of charge at https://pubs.acs.org/doi/10.1021/acsami.6c07675.

Additional experimental details and supplementary results, including the growth scheme, optical microscopy, temperature-dependent degradation images, comparative XPS spectra, long-term PL stability data, MoS_2 capping results, PGA temperature dependence, and additional SEM/STEM images (PDF)

■ AUTHOR INFORMATION

Corresponding Author

Won Il Park − *Division of Materials Science and Engineering, Hanyang University, Seoul 04763, Republic of Korea;* orcid.org/0000-0001-8312-4815; Email: wipark@hanyang.ac.kr

Authors

Lia Saptini Handriani − *Division of Materials Science and Engineering, Hanyang University, Seoul 04763, Republic of Korea*

Hyeonsu Park − *Division of Materials Science and Engineering, Hanyang University, Seoul 04763, Republic of Korea*

Zhe Gao − *Division of Materials Science and Engineering, Hanyang University, Seoul 04763, Republic of Korea*

Jae-il Jang − *Division of Materials Science and Engineering, Hanyang University, Seoul 04763, Republic of Korea;* orcid.org/0000-0003-4526-5355

https://doi.org/10.1021/acsami.6c07675
ACS Appl. Mater. Interfaces 2026, 18, 39417−39428

Complete contact information is available at:
https://pubs.acs.org/10.1021/acsami.6c07675

Author Contributions

W.I.P. conceived the study and provided overall research supervision. L.S.H. designed and performed the MOCVD growth experiments and optical characterizations and led the data analysis. H.P., Z.G., and J.J. contributed to sample preparation and experimental data analysis. L.S.H. and W.I.P. cowrote the manuscript. All authors reviewed and approved the final manuscript.

Notes

The authors declare no competing financial interest.

■ ACKNOWLEDGMENTS

This work was supported by the National Research Foundation (NRF) of Korea funded by the Ministry of Science, ICT and Future Planning (MSIP) of Korea (Nos. RS-2021-NR060087 and RS-2024-00353762).

■ REFERENCES

(1) Duan, X.; Zhang, H. Introduction: two-dimensional layered transition metal dichalcogenides. *Chem. Rev.* **2024**, *124*, 10619−10622.
(2) Bianchi, M. G.; Risplendi, F.; Re Fiorentin, M.; Cicero, G. Engineering the electrical and optical properties of WS_2 monolayers via defect control. *Adv. Sci.* **2024**, *11* (4), 2305162.
(3) Kim, Y.; Kim, B.; Jang, S.; Kim, M.; Saptini, H. L.; An, S. J.; Park, W. I. Comparative Investigation of Interplay Between Photothermoelectric and Photoconductive Effects in MoS_2 Devices. *ACS Appl. Electron. Mater.* **2023**, *5* (12), 6824−6831.
(4) Yun, H.; Park, H.; Kim, Y.; Handriani, L. S.; Jeong, D.; Jang, S.; Park, W. I. Position-Selective MoS_2 Photoresponse Dynamics for In-Sensor Encoding of Motion History. *ACS Appl. Electron. Mater.* **2026**, *8*, 3207−3217.
(5) Aggarwal, V.; Abidi, I. H.; Limb, J.; Kofler, C.; Verma, A. K.; Giridhar, S. P.; Dissanayake, N. S.; Vashishtha, P.; Tollerud, J. O.; Mao, J. Stacking Mode-Driven Enhancement of Optoelectronic and Electrocatalytic Properties in Bilayer 2H MoS_2. *ACS Appl. Mater. Interfaces* **2025**, *17* (34), 48658−48669.
(6) Mawlong, L. P.; Hoang, A. T.; Chintalapalli, J.; Ji, S.; Lee, K.; Kim, K.; Ahn, J.-H. Reduced defect density in MOCVD-grown MoS_2 by manipulating the precursor phase. *ACS Appl. Mater. Interfaces* **2023**, *15* (40), 47359−47367.
(7) Wang, W.; Shu, H.; Wang, J.; Cheng, Y.; Liang, P.; Chen, X. Defect passivation and photoluminescence enhancement of monolayer MoS_2 crystals through sodium halide-assisted chemical vapor deposition growth. *ACS Appl. Mater. Interfaces* **2020**, *12* (8), 9563−9571.
(8) Ahn, B.; Ahn, J.; Kim, M.; Lim, S. C.; Ji, H. Achieving quasi intrinsic MoS2 performance via liquid-based neutralization of material and interface defects with H^+ protons. *ACS Appl. Mater. Interfaces* **2024**, *16* (49), 68553−68561.
(9) Peimyoo, N.; Yang, W.; Shang, J.; Shen, X.; Wang, Y.; Yu, T. Chemically driven tunable light emission of charged and neutral excitons in monolayer WS_2. *ACS Nano* **2014**, *8* (11), 11320−11329.
(10) Wang, Y. H.; Ho, H. M.; Ho, X. L.; Lu, L. S.; Hsieh, S. H.; Huang, S. D.; Chiu, H. C.; Chen, C. H.; Chang, W. H.; White, J. D. Photoluminescence enhancement in WS_2 nanosheets passivated with oxygen ions: Implications for selective area doping. *ACS Appl. Nano Mater.* **2021**, *4* (11), 11693−11699.
(11) Wen, X.; Gong, Z.; Li, D. Nonlinear optics of two-dimensional transition metal dichalcogenides. *InfoMat* **2019**, *1* (3), 317−337.
(12) Mukherjee, S.; Wang, S.; Venkatakrishnarao, D.; Tarn, Y.; Talha-Dean, T.; Lee, R.; Verzhbitskiy, I. A.; Huang, D.; Mishra, A.; John, J. W. Toward phonon-limited transport in two-dimensional transition metal dichalcogenides by oxygen-free fabrication. *ACS Nano* **2025**, *19* (9), 9327−9339.
(13) Zhang, Y.; Yao, Y.; Sendeku, M. G.; Yin, L.; Zhan, X.; Wang, F.; Wang, Z.; He, J. Recent progress in CVD growth of 2D transition metal dichalcogenides and related heterostructures. *Adv. Mater.* **2019**, *31* (41), 1901694.
(14) Hong, S. C.; Baek, J.-H.; Kim, J.; Lee, H.; Lee, G.-H. Strain-Mediated Control of Domain Structures in 3R-MoS_2 Bilayers Synthesized by Vapor−Liquid−Solid Growth in Chemical Vapor Deposition. *ACS Nano* **2025**, *19* (33), 30487−30494.
(15) Li, S. Salt-assisted chemical vapor deposition of two-dimensional transition metal dichalcogenides. *iScience* **2021**, *24* (11), No. 103229.
(16) Chang, Y.-P.; Li, W.-B.; Yang, Y.-C.; Lu, H.-L.; Lin, M.-F.; Chiu, P.-W.; Lin, K.-I. Oxidation and degradation of WS_2 monolayers grown by NaCl-assisted chemical vapor deposition: mechanism and prevention. *Nanoscale* **2021**, *13* (39), 16629−16640.
(17) Qin, B.; Ma, C.; Guo, Q.; Li, X.; Wei, W.; Ma, C.; Wang, Q.; Liu, F.; Zhao, M.; Xue, G. Interfacial epitaxy of multilayer rhombohedral transition-metal dichalcogenide single crystals. *Science* **2024**, *385* (6704), 99−104.
(18) Jung, Y.; Moon, D.; Joo, J.; Kim, J.; Oh, S.; Lee, H.; Kim, J.; Kim, H.; Ryu, H.; Hong, S. C. WO_x-driven growth of 2H-and 3R-WS_2 multilayers by physical vapor deposition. *Appl. Surf. Sci.* **2025**, *682*, No. 161676.
(19) Yang, R.; Feng, S.; Lei, X.; Mao, X.; Nie, A.; Wang, B.; Luo, K.; Xiang, J.; Wen, F.; Mu, C. Effect of layer and stacking sequence in simultaneously grown 2H and 3R WS_2 atomic layers. *Nanotechnology* **2019**, *30* (34), 345203.
(20) Xu, M.; Ji, H.; Zhang, M.; Zheng, L.; Li, W.; Luo, L.; Chen, M.; Liu, Z.; Gan, X.; Wang, X. CVD synthesis of twisted bilayer WS_2 with tunable second harmonic generation. *Adv. Mater.* **2024**, *36* (19), 2313638.
(21) Baek, J.-H.; Kim, H. G.; Lim, S. Y.; Hong, S. C.; Chang, Y.; Ryu, H.; Jung, Y.; Jang, H.; Kim, J.; Zhang, Y. Thermally induced atomic reconstruction into fully commensurate structures of transition metal dichalcogenide layers. *Nat. Mater.* **2023**, *22* (12), 1463−1469.
(22) Kieczka, D.; Bussolotti, F.; Maddumapatabandi, T. D.; Bosman, M.; Shluger, A.; Regoutz, A.; Goh, K. E. J. Unveiling surface dynamics: in situ oxidation of defective WS_2. *Nanoscale* **2025**, *17* (16), 10082−10094.
(23) Karger, L.; Synnatschke, K.; Settele, S.; Hofstetter, Y. J.; Nowack, T.; Zaumseil, J.; Vaynzof, Y.; Backes, C. The Role of Additives in Suppressing the Degradation of Liquid-Exfoliated WS_2 Monolayers. *Adv. Mater.* **2021**, *33* (42), 2102883.
(24) Nakagawa, Y.; Shiratsuchi, Y.; Shibayama, T.; Takeguchi, M. Ultraviolet Light-Induced Surface Changes of Tungsten Oxide in Air: Combined Scanning Transmission Electron Microscopy and X-ray Photoelectron Spectroscopy Analysis. *Nanomaterials* **2024**, *14* (18), 1486.
(25) Li, H.; Abdelgaid, M.; Paudel, J. R.; Holzapfel, N. P.; Augustyn, V.; McKone, J. R.; Mpourmpakis, G.; Crumlin, E. J. Operando unveiling of hydrogen spillover mechanisms on tungsten oxide surfaces. *J. Am. Chem. Soc.* **2025**, *147* (8), 6472−6479.
(26) Bussolotti, F.; Kawai, H.; Maddumapatabandi, T. D.; Fu, W.; Khoo, K. H.; Goh, K. E. J. Role of S-vacancy concentration in air oxidation of WS_2 single crystals. *ACS Nano* **2024**, *18* (12), 8706−8717.
(27) Yang, H.; Wang, Y.; Zou, X.; Bai, R.; Wu, Z.; Han, S.; Chen, T.; Hu, S.; Zhu, H.; Chen, L. Wafer-scale synthesis of WS_2 films with in situ controllable p-type doping by atomic layer deposition. *Research* **2021**, *9*, 9862483.
(28) Seo, S.; Kim, S.; Choi, H.; Lee, J.; Yoon, H.; Piao, G.; Park, J. C.; Jung, Y.; Song, J.; Jeong, S. Y. Direct in situ growth of centimeter-scale multi-heterojunction $MoS_2/WS_2/WSe_2$ thin-film catalyst for photo-electrochemical hydrogen evolution. *Adv. Sci.* **2019**, *6* (13), 1900301.
(29) Gao, Y.; Lu, S.; Hou, X.; Wang, B.; Jiang, Z.; Wang, Y.; Fang, T. Salt-assisted growth of rhombohedral 3R-MoS_2 single-crystal with

enhanced electrocatalytic hydrogen evolution reaction performance. *J. Colloid Interface Sci.* **2025**, *700*, No. 138559.
(30) Zeng, Z.; Sun, X.; Zhang, D.; Zheng, W.; Fan, X.; He, M.; Xu, T.; Sun, L.; Wang, X.; Pan, A. Controlled vapor growth and nonlinear optical applications of large-area 3R phase WS_2 and WSe_2 atomic layers. *Adv. Funct. Mater.* **2019**, *29* (11), 1806874.
(31) Shin, J. H.; Jang, S.; Kim, S. H.; Chang, W. J.; Kim, J.; Yang, S. I.; Park, W. I. Imaging and analysis of multidimensional atomically thin transition metal dichalcogenide layers on diatom frustules. *Appl. Surf. Sci.* **2022**, *577*, No. 151876.
(32) Jang, S.; Handriani, L. S.; Yun, H. C.; Jeong, D. Y.; Kim, Y.; Kim, M.; Gao, Z.; Jang, J.-i.; Park, W. I. Direct and Scalable Edge-Induced Alloying of $Mo_{1-x}W_xS_2$ via Patterned MoS_2 Templates. *Mater. Res. Bull.* **2026**, *197*, No. 113942.
(33) Handriani, L. S.; Jang, S.; Kim, Y.; Yun, H.; Jeong, D. Y.; Park, H.; Gao, Z.; Jang, J.-i.; Park, W. I. Substrate-field-modulated remote-van der Waals hybrid epitaxy in transition metal dichalcogenide heterostructures. *Nano Converg.* **2026**, *13* (1), 12.
(34) Kerherve, G.; Skinner, W. S.; Hochhaus, J. A.; Graf, A.; Morgan, D. J.; Isaacs, M. A.; Reed, B. P.; Nakajima, H.; Payne, D. J. KherveFitting: An open source software for fitting X-ray photoelectron spectroscopy data. *Surf. Interface Anal.* **2026**, *58* (1), 54−65.
(35) Liu, L.; Li, T.; Gong, X.; Wen, H.; Zhou, L.; Feng, M.; Zhang, H.; Zou, N.; Wu, S.; Li, Y. Homoepitaxial growth of large-area rhombohedral-stacked MoS_2. *Nat. Mater.* **2025**, *24* (8), 1195−1202.
(36) Chen, J.; Guo, Y.; Zhang, Y.; Li, Z.; Guo, Q.; Yang, Q.; Li, K.; Zhang, Y.; Zhang, B.; Hu, Y. Growth of rhombohedral-stacked single-crystal WS_2/MoS_2 vertical heterostructures. *Nat. Commun.* **2026**, *17*, 2172.
(37) Barthel, J. Dr. Probe: A software for high-resolution STEM image simulation. *Ultramicroscopy* **2018**, *193*, 1−11.
(38) Giannozzi, P.; Baroni, S.; Bonini, N.; Calandra, M.; Car, R.; Cavazzoni, C.; Ceresoli, D.; Chiarotti, G. L.; Cococcioni, M.; Dabo, I. QUANTUM ESPRESSO: a modular and open-source software project for quantum simulations of materials. *J. Phys.: Condens. Matter* **2009**, *21* (39), 395502.
(39) Giannozzi, P.; Andreussi, O.; Brumme, T.; Bunau, O.; Buongiorno Nardelli, M.; Calandra, M.; Car, R.; Cavazzoni, C.; Ceresoli, D.; Cococcioni, M. Advanced capabilities for materials modelling with Quantum ESPRESSO. *J. Phys.: Condens. Matter* **2017**, *29* (46), 465901.
(40) Perdew, J. P.; Burke, K.; Ernzerhof, M. Generalized gradient approximation made simple. *Phys. Rev. Lett.* **1996**, *77* (18), 3865.
(41) Blöchl, P. E. Projector augmented-wave method. *Phys. Rev. B* **1994**, *50* (24), 17953.
(42) Grimme, S.; Antony, J.; Ehrlich, S.; Krieg, H. A consistent and accurate ab initio parametrization of density functional dispersion correction (DFT-D) for the 94 elements H-Pu. *J. Chem. Phys.* **2010**, *132* (15), 154104.
(43) Grimme, S.; Ehrlich, S.; Goerigk, L. Effect of the damping function in dispersion corrected density functional theory. *J. Comput. Chem.* **2011**, *32* (7), 1456−1465.
(44) Henkelman, G.; Arnaldsson, A.; Jónsson, H. A fast and robust algorithm for Bader decomposition of charge density. *Comput. Mater. Sci.* **2006**, *36* (3), 354−360.

https://doi.org/10.1021/acsami.6c07675
ACS Appl. Mater. Interfaces 2026, 18, 39417−39428